Telomere-Centromere–Driven Genomic Instability Contributes to Karyotype Evolution in a Mouse Model of Melanoma[1,2]

Amanda Gonçalves dos Santos Silva*,
Herbert Alexander Graves†, Amanda Guffei†,
Tatiana Iervolino Ricca*, Renato Arruda Mortara*,
Miriam Galvonas Jasiulionis*,‡ and Sabine Mai†

*Department of Microbiology, Immunology, and
Parasitology, Universidade Federal de São Paulo-UNIFESP,
São Paulo, SP, Brazil; †Manitoba Institute of Cell
Biology, The University of Manitoba, Cancer Care
Manitoba, Winnipeg, Manitoba, Canada; ‡Department
of Pharmacology, Universidade Federal de São Paulo,
São Paulo, Brazil

Abstract
Aneuploidy and chromosomal instability (CIN) are hallmarks of most solid tumors. These alterations may result from inaccurate chromosomal segregation during mitosis, which can occur through several mechanisms including defective telomere metabolism, centrosome amplification, dysfunctional centromeres, and/or defective spindle checkpoint control. In this work, we used an *in vitro* murine melanoma model that uses a cellular adhesion blockade as a transforming factor to characterize telomeric and centromeric alterations that accompany melanocyte transformation. To study the timing of the occurrence of telomere shortening in this transformation model, we analyzed the profile of telomere length by quantitative fluorescent *in situ* hybridization and found that telomere length significantly decreased as additional rounds of cell adhesion blockages were performed. Together with it, an increase in telomere-free ends and complex karyotypic aberrations were also found, which include Robertsonian fusions in 100% of metaphases of the metastatic melanoma cells. These findings are in agreement with the idea that telomere length abnormalities seem to be one of the earliest genetic alterations acquired in the multistep process of malignant transformation and that telomere abnormalities result in telomere aggregation, breakage-bridge-fusion cycles, and CIN. Another remarkable feature of this model is the abundance of centromeric instability manifested as centromere fragments and centromeric fusions. Taken together, our results illustrate for this melanoma model CIN with a structural signature of centromere breakage and telomeric loss.

Neoplasia (2010) 12, 11–19

Introduction
The progression of a melanocyte to malignant melanoma is a multistep process requiring the gradual acquisition of genetic and epigenetic alterations. This transformation process is characterized by the loss of tumor-suppressor genes, epigenetic changes, alterations of the mismatch repair pathway, and the generation of genomic instability [1]. Malignant melanomas commonly display two types of genomic instability found in cancer, microsatellite instability and chromosomal instability (CIN). Microsatellite instability is found in approximately 30% of cases, whereas CIN is associated with most cases analyzed [1–3].

CIN is a hallmark of most classes of solid tumors [2–6]. Its initiation may be the result of inaccurate chromosomal segregation during mitosis caused in part by defective telomere metabolism, centromere

amplifications, dysfunctional centromeres, or defective spindle checkpoint controls [7,8]. Centromere-driven CIN is resultant from a variety of insults to the centromere that impact in part or cumulatively on the assembly of the kinetochore, segregation of the sister chromatids, nuclear localization of centromeres, and recombination events at pericentromeric regions [9–11]. Pericentromeric regions are often hotspots for both recombination events during evolution [12] and in cancer [10,13]. Centromere integrity is therefore essential for genomic stability, and there are several examples where defects in centromere function are associated with birth defects, spontaneously aborted fetuses, Robertsonian (Rb) translocations, and cancers (for review, see Gonçalves dos Santos Silva et al. [11]). In addition, pericentric inversions in humans are often associated with decreased male fertility [14–16], cancer [17–19], and mental retardation [20,21]. The centromeres are also substrates for rearrangements that are associated with structural genetic abnormalities in cancer where, in the same fashion as evolution, selection occurs at the cellular level in an accelerated manner (for review, see Gonçalves dos Santos Silva et al. [11]).

Telomere dysfunction resulting from eroded or unprotected telomere structures has been shown to induce CIN [22,23]. Unprotected telomeres whether through erosion by progressive cell division or telomere capping malfunction have been shown to recombine and illegitimately repair through the nonhomologous end joining double-strand break repair pathway [24]. Such illegitimate telomeric repair is known to generate telomere fusions and aggregates that form chromosomal bridges leading to continued rounds of double-strand break creation and mutational repair [25–28].

In melanoma, the possibility of correlating a specific pathological stage with corresponding genetic alterations has allowed the experimental study of different stages of tumor progression, but until now, most experimental models of tumorigenesis use chemical or environmental carcinogens and genetic manipulations to study the progression of this disease (for reviews, see Foijer et al. [29] and Wu and Pandolfi [30]). Here, we used an experimental model of melanocyte malignant transformation that uses forced sequential cycles of adhesion blockage as a transforming factor in which the nontumorigenic melanocyte lineage melan-a was cultured in suspension for 96 hours [31]. Progressive morphologic alterations were observed along each cycle of anchorage blockage culminating in the establishment of nontumorigenic melan-a sublines corresponding to intermediate phases of malignant transformation found after two and four cycles of anchorage blockage (2C and 4C lineages, respectively). In addition, distinct tumorigenic lineages, both slow-growing (4C3–) and fast-growing melanoma lineages (4C3+) were established from spheroids formed after a new anchorage blockade cycle of 4C cells. Oncogenic cell signaling pathways generated through sequential anchorage blockage cycles offer a novel opportunity to study the mechanisms for the decline of genomic integrity specifically in melanoma. Our study suggests that this transformation is driven by changes in telomere length and stability, centromere stability, and overall karyotype evolution.

Materials and Methods

Cells and Cell Culture Conditions

The nontumorigenic murine melanocyte lineage, melan-a was grown in RPMI (pH 6.9; Gibco, Carlsbad, CA), supplemented with 5% fetal bovine serum (Gibco) and 200 nM 12-o-tetradecanoyl phorbol-13-acetate (Tocris, Ellisville, MO) at 37°C in a humidified atmosphere and 5% CO_2. Melan-a cell sublines 2C, 4C, 4C3–, and 4C3+, established after submitting melan-a cells to sequential substrate adhesion impediment cycles, were cultured using the same conditions as the parental cell line but without the addition of 12-o-tetradecanoyl phorbol-13-acetate. The melan-a cell line appears in this work as a near triploid cell with a median of 54 chromosomes, which is probably a result of the time in culture because this cell line has first been described as having a normal diploid karyotype [32]. Cells were maintained at a density of around 10^5 to 10^6 cells/ml.

Cell Fixation and Chromosome Preparations

Cells were harvested and spun down at 800 rpm for 10 minutes, and for chromosome preparation, they were resuspended in 5 ml of 0.075 M KCl for 30 minutes at room temperature. For chromosome fixation, the drop fixation method [33] was used. For the fixation of three-dimensional interphase nuclei, all cells were cultured on glass slides until subconfluence and three-dimensionally fixed using 3.7% formaldehyde/phosphate-buffered saline for 15 minutes at room temperature.

Immunofluorescence

Different cell lines were cultured on glass coverslips (Glasstécnica, Sao Paulo, Brazil) until subconfluence and fixed in 1% paraformaldehyde in PBS. Fluorescent detection of c-Myc protein was performed as described in Garagna et al. [34] by using a polyclonal anti–c-Myc antibody (N262; Santa Cruz Biotechnology, Santa Cruz, CA) and a goat antirabbit immunoglobulin G fluorescein isothiocyanate (FITC) antibody, at 1:100 and 1:1000 dilutions, respectively. Analysis was performed by using a Bio-Rad 1024 UV confocal system attached to a Zeiss Axiovert 100 microscope (Carl Zeiss, Inc., Canada), with a 63×/1.4 oil objective lens.

Quantitative Fluorescence In Situ Hybridization

On slides with three-dimensional interphase nuclei fixed, telomere fluorescence in situ hybridization (FISH) protocol was performed as described above by using Cy3-labeled peptide nucleic acid (PNA) probes (DAKO, Glostrup, Denmark). At least 30 nuclei were analyzed for each cell line. AXIOVISION 4.6 (Carl Zeiss) with deconvolution module was used. For every fluorochrome, the final three-dimensional images consist of a stack of 50 individual images with a sampling distance of 200 nm along the z and 107 nm in the xy direction. Three-dimensional image acquisition was performed on at least 30 nuclei per cell line using an AxioImager Z1 microscope (Carl Zeiss) and an AxioCam HR charge-coupled device (Carl Zeiss) with a 63×/1.4 oil objective lens (Carl Zeiss). The constrained iterative algorithm was used for deconvolution [35]. Note that telomeric signals at a distance of 200 nm or less will be detected as one signal [36]. Telomere measurements were done with TELOVIEW version 2.3 [37].

Fluorescent In Situ Hybridization

PNA-FISH was performed on two-dimensional metaphase samples derived from T38Ha primary mouse fibroblasts, melan-a, 4C3–, and 4C3+. A Cy3-labeled PNA telomeric probe was purchased from DAKO, and a PNA human centromeric probe (Applied Biosystems, Foster City, CA) was custom-made. The sequences and the method description were described elsewhere [38]. Additional FISH experiments were performed using metaphase chromosomes of the 4C3– cell line and a mouse pan-centromeric probe conjugated with FITC from Cambio (Dry Drayton, Cambridge, UK). The experiment was carried

out as described by Mai and Wiener [33]. All slides were imaged the following morning to avoid changes in imaging conditions. Three-dimensional image acquisition was performed on 20 metaphases per sample using an Axioplan 2 microscope (Carl Zeiss) and an AxioCam HR charge-coupled device (Carl Zeiss) with a 63×/1.4 oil objective lens (Carl Zeiss).

Spectral Karyotyping Analysis

Spectral karyotyping (SKY) was performed using the ASI (Applied Spectral Imaging, Vista, CA) kit for mice in accordance with the supplier's hybridization protocols. We used the Spectra Cube (ASI) on an Axioplan 2 microscope (Carl Zeiss) with a 63×/1.4 oil objective and the Case Data Manager 4.0 software (ASI) for PC to perform analyses. A minimum of 20 metaphases was examined for each cell line.

Proliferation Rates Index – 3-(4,5-Dimethylthiazol-2-yl)-2, 5-diphenyltetrazolium Bromide Assay

For measurements of cell viability, 2.5×10^3 cells/100 µl medium were plated into each well of 96-well plates. After 24, 48, 72, or 96 hours of incubation, 10 µl of 3-(4,5-dimethylthiazol-2-yl)-2,5-diphenyltetrazolium Bromide (MTT) solution (Calbiochem, Darmstadt, Germany) was added into each well, and plates were incubated for 4 hours at 37°C, and 450 nm UV absorbance of each sample was measured in a microplate reader. The assay was done in triplicate wells, and $P < .05$ was considered significant.

Tumorigenicity Assay

Cells were harvested after trypsin treatment of subconfluent monolayers, counted, and then suspended in 1× PBS. Melan-a cells and their derived clones (1×10^6 cells) were injected subcutaneously in the flank of syngeneic 6- to 8-week-old C57Bl/6 female mice and determined as follows: [maximum diameter × (minimum diameter)2] / 2. Animals were kept under 12-hour daylight cycles, without food or water restriction, and checked daily for tumor development. Each experimental group consisted of at least five animals (CEP 0738.07). The P value for the overall study was less than .001.

Experimental Metastasis Assay

Cells of subconfluent cultures were trypsinized, suspended in RPMI with 10% fetal calf serum, spin down, suspended in PBS, counted, and adjusted to the necessary concentration. Cells (2×10^5) in 0.1 ml of PBS were injected into the lateral tail vein of syngeneic C57BL/6 female mice with a 27-gauge needle. Lungs were harvested 20, 40, 60, and 80 days later, and metastatic foci in the lungs were identified. The experimental groups consisted of 15 animals for the 4C3– cell line and 7 for the 4C3+ cell line.

Telomeric Repeat Amplification Protocol

Telomerase activity of cell lysates was analyzed by the telomeric repeat amplification protocol assay with a TRAPeze Telomerase Detection Kit-S7700 (Chemicon, Millipore, Billerica, MA) according to the manufacturer's instructions. Each reaction was carried out by using 0.05 µg of extract. Polymerase chain reaction (PCR) products were electrophoresed in a 12.5% acrylamide gel (0.5 × TBE (Tris/borate/EDTA) buffer using the PROTEAN II xi gel system (Biorad, Hercules, CA). Gels were silver-stained according to the protocol described elsewhere [39]. Images were captured by using FinePix S9000 digital camera (Fujifilm, Minato, Tokio, Japan).

Reverse Transcription–PCR

Total RNA was isolated from cells with TRizol (Invitrogen, Carlsbad, CA). One microgram of RNA was reverse-transcribed to complementary DNA with Superscript III (Invitrogen). The resulting single-strand complementary DNA were amplified by PCR in a reaction mixture containing 75 mM Tris-HCl pH 9.0, 2 mM $MgCl_2$, 50 mM KCl, 20 mM $(NH_4)_2SO_4$, 0.4 mM of each deoxynucleotide triphosphate, 0.4 µM of each primer, 1 U of BioTools DNA Polymerase – recombinant from *Thermus thermophilus* (BioTools, Madrid, Spain). The thermal cycling conditions were as follows: initial 5 minutes at 94°C, followed by cycles (30 for Tert and 20 for β-actin amplifications) of 94°C for 45 seconds, 65°C for 45 seconds, and 72°C for 60 seconds. The β-actin messenger RNA was used as control. PCR fragment amplification was confirmed by 1% agarose gel. The PCR primers were as follows: Tert forward 5′CATGGGTGCCAAGTCCTGCTC3′; Tert reverse 5′CTGTGCAGGCGGAGCAAATCC3′; actin forward 5′CGAGGCCCAGAGCAAGAGAG3′; actin reverse 5′AGGAAGAG-GATGCGGCAGTGG 3′.

Statistical Analysis

A Student's t test with two tails was used to calculate the statistical significance of the observed differences in telomere length. To calculate the differences in c-Myc and Tert expression, the band intensities were quantified using ImageJ 1.38 software (Image Processing and Analysis in JAVA, Wayne Rasband, National Institutes of Health, Bethesda, MD, http://rsb.info.nih.gov/ij/), and P values were determined by one-way analysis of variance. To calculate the statistical significance of the proliferation index and tumorigenesis assay, one-way analysis of variance was used with Tukey's post test. For the comparison of survival curves, log-rank test was performed. For chromosome rearrangements and changes in ploidy, we used nonparametric Kruskal-Wallis with Dunn's post test. GraphPad Prism version 4.00 for Windows (GraphPad Software, San Diego, CA, www.graphpad.com) was used for the all calculations.

Results

Characterization of Our Mouse Melanoma Model

Cell viability and proliferation rates were characterized using the colorimetric MTT assay. The nontumorigenic cells (melan-a, 2C, and 4C) showed a similar *in vitro* proliferation rate. The tumorigenic cell lines 4C3– and 4C3+ showed a higher proliferative ability than melan-a, 2C, and 4C ($P < .0001$; Figure 1*A*). All cell lines constitutively expressed c-Myc protein (Figure W2). Owing to these significant differences in the cell proliferation *in vitro*, we examined the consequences of their different proliferation rates *in vivo*. As predicted and previously described, melan-a, 2C, and 4C did not cause tumor formation [31,40], whereas the injection of 4C3– cells led to tumor formation with a growth rate roughly less than half of tumors produced by the inoculation of 4C3+ cells (Figure 1*B*). In addition, the latency time for tumor development after inoculation of the 4C3– cell line was almost twice the time of 4C3+ being 25 and 14 days, respectively (Figure 1*C*).

Next, we determined the metastatic capacity of 4C3– and 4C3+ cell lines. A total of 2×10^5 cells were inoculated intravenously, and lungs were harvested 20, 40, 60, and 80 days later to check for metastatic foci. After just 20 days, every animal that was inoculated with 4C3+ cell lines had several metastatic foci in their lungs (Figure 1*D*,
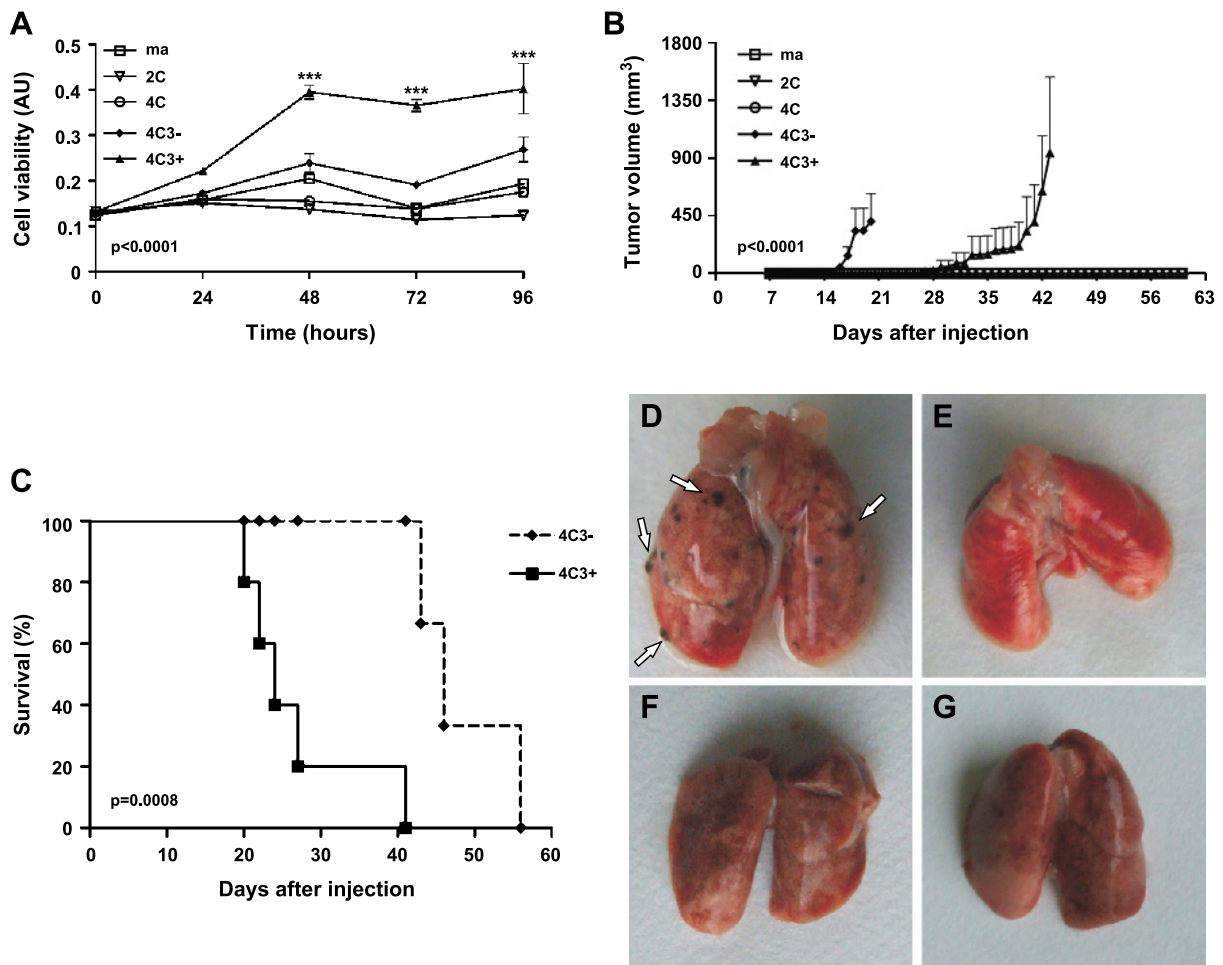
Figure 1. Characteristics of the mouse melanoma model. (A) Cell viability was determined by the MTT assay in triplicate. (B) Tumorigenicity assay *in vivo*. Mice were subcutaneously injected with 2×10^5 cells. *Bars:* SD of the mean of five animals per group. ***$P <$ .0001. (C) Survival curves (100% × number of mice alive after each day / total number of mice at day 0) for mice inoculated with 4C3− and 4C3+. Experimental metastasis assay: 2×10^5 4C3+ cells (D) and 4C3− (E, F, and G) were injected through the caudal vein. Mice were killed 20 (D and E), 40 (F), and 80 (G) days later; their lungs were removed; and metastatic foci in the lungs were identified and some are indicated in panel D by the white arrows. *ma* indicates melan-a cells; *2C and 4C*, melan-a cells submitted to two and four substrate adhesion blockade cycles, respectively; *4C3−*, slow-growing melanoma cell line; *4C3 +*, fast-growing melanoma cell line.

white arrows). Conversely, metastatic foci were not found in the lungs of animals that were inoculated with 4C3− cell line even 80 days after injection (Figure 1, *E–G*).

Telomere Shortening in the Presence of TERT Expression and Telomerase Activity

To analyze the telomere length on our model, we performed quantitative FISH (Q-FISH) on three-dimensionally fixed interphase nuclei with a Cy3 telomeric PNA probe. To this end, 30 nuclei were analyzed per cell line. Telomere length progressively decreased through the melanoma genesis model as illustrated by the column scatter graph in Figure 2*A*. The immortalized cell line, melan-a, and the nontumorigenic cell line (2C and 4C) showed highly heterogeneous telomeres sizes, whereas we noted a smaller difference in size distribution in the tumorigenic ones (4C3− and 4C3). In comparison to the parental cell (melan-a), the variation in telomere length was very significant for 2C ($P <$ .0005), significant for 4C ($P <$ .009), and highly significant for 4C3− and 4C3+ ($P <$ .0001). In all cases, the differences in telo-

mere length with respect to the metastatic melanoma cell line (4C3+) were highly significant ($P <$ .0001).

The differences found in telomere length prompted us to analyze the telomerase activity in the model (Figure 2*B*). Because the Tert subunit seems to be the main rate-limiting determinant of telomerase and it has been suggested to be an indicator of its activity [41,42], we opted to analyze the expression of this gene by reverse transcription–PCR. Tert was then quantified for all cell lines involved in this study, and no statistical differences among the cells were found (Figure 2*C*).

The loss of telomere-specific FISH signals was examined using the telomere probe in metaphase spreads of primary cultures of mouse T38Ha primary fibroblasts (used as a normal control—data not shown), melan-a (data not shown), and on the nonmetastatic and metastatic melanoma cell lines (4C3− and 4C3+, respectively; Figure 3).

All cell lines but the normal control displayed marked loss of telomere-specific signals, when compared with the control ($P <$ .0001). The highest number of signal free ends was observed in 4C3+ where more than 30% of the ends had no distinguishable telomere signal ($P <$ .001). Whereas melan-a showed telomere free ends on 9% of potential telomere
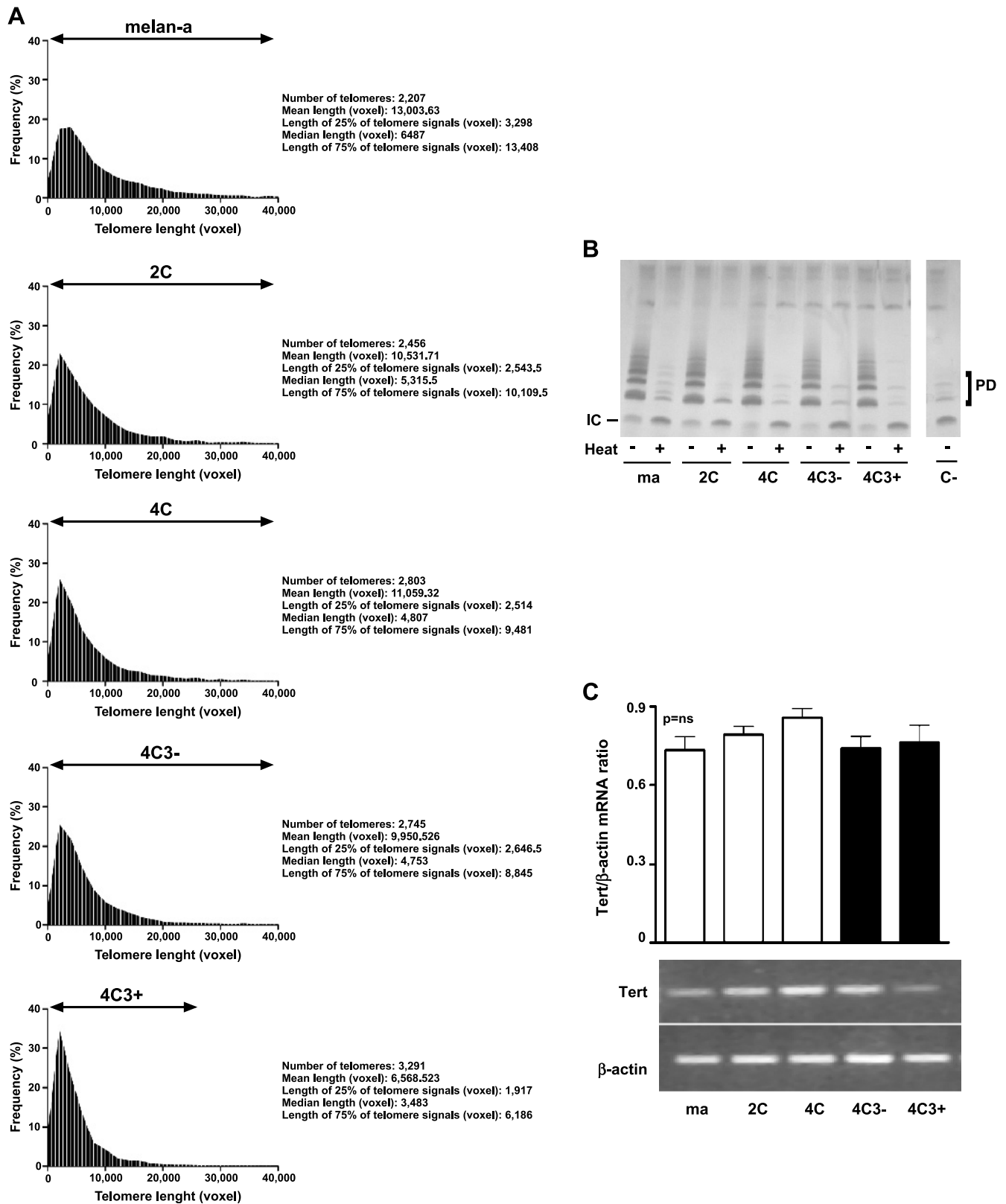
Figure 2. Shortening of telomeres in the presence of telomerase activity. (A) Telomere length distribution in the model as determined by PNA telomere Q-FISH. The vertical lines and the arrows highlight the decreased heterogeneity of telomere lengths through the melanoma genesis model. (B) Telomerase activity in the model by the TRAP assay. (−) Non-heated extract, (+) heated extract, IC: internal PCR control, C−: negative control and PD: primer dimers. (C) Tert expression analyzed in melan-a cells and melan-a–derived cell lines by reverse transcription–PCR. β-Actin expression was used as a normalization control. No significant difference was observed between the samples. *ma* indicates melan-a cells; *2C and 4C*, melan-a cells submitted to two and four substrate adhesion blockade cycles, respectively; *4C3−*, slow-growing melanoma cell line; *4C3+*, fast-growing melanoma cell line.
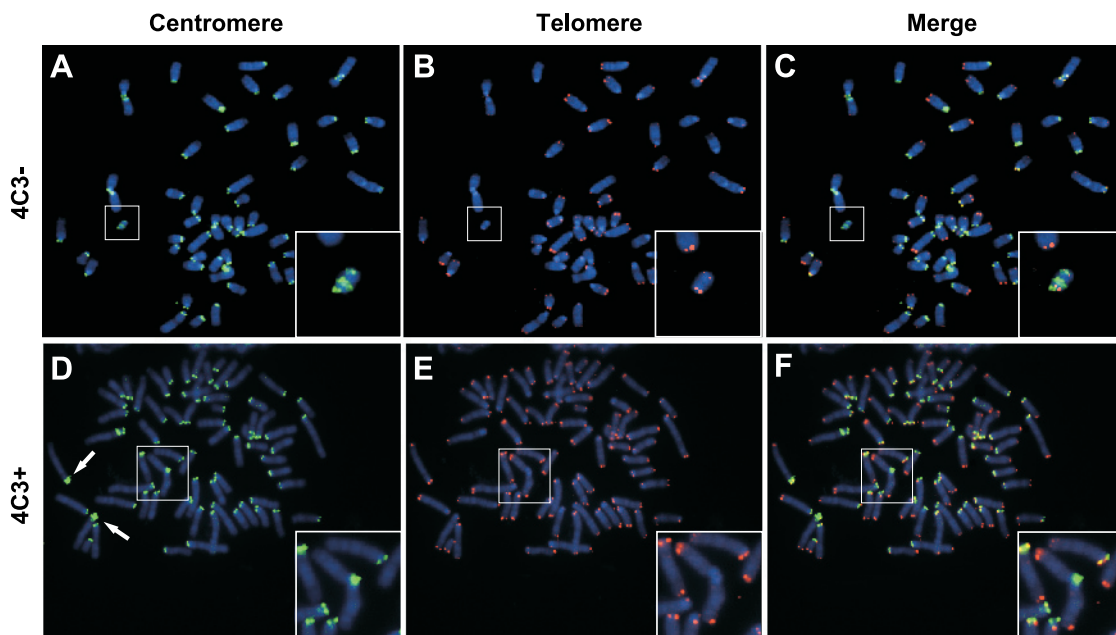
Figure 3. Rb fusions and centromere abnormalities. Representative FISH images of 4C3− and 4C3+ metaphases hybridized with probes against centromere and telomere. 4C3− cell line is shown in panels A, B, and C. Note the centromere fragment in the magnification box; it shows under the centromere staining (A) four telomeric signals (B) and the merge image (C). (D, E, and F) Representative metaphase of the 4C3+ cell line. Rb fusion is shown on the magnification boxes. Note that under the centromeric fusion point (D), there are no telomeric signals (E). (A and D) Centromeric signals only. (B and E) Telomeric signals only. Note that in both cell lines, chromosomes with missing signals are present, but 4C3+ had the highest percentage of telomere free ends (see text). *4C3−* indicates slow-growing melanoma cell line; *4C3 +*, fast-growing melanoma cell line.

signals ($P < .05$), the nonmetastatic cell line 4C3– showed telomere free ends on 15% ($P < .001$). All together, these results indicate ongoing telomeric instability in this model.

Centromere Instability and Fragmentation

In our work, centromeric fragments were first observed by dual-color FISH (Figure 3A) and by inverted 4′,6-diamidino-2-phenylindole during the SKY analysis (Figure W1). To confirm these observations, a mouse centromeric probe was then hybridized against the same slides used for SKY. The centromere hybridization matched the structures previously identified by inverted 4′,6-diamidino-2-phenylindole (Figure 4, A and B). The number of centromere fragments increased from melan-a to 4C3, becoming negligible in 4C3+ ($P < .0001$; Figure 4C).

Some of the centromere fragments showed features of mini chromosomes or double minutes containing four telomeric signals (Figure 3B). In addition, a nonrandom Rb translocation was noted in 4C3+ cells involving only chromosomes 8 and 12 (Table W1), suggesting either nonrandom centromere instability or a selective proliferation advantage of cells carrying this Rb chromosome combination during the acquisition of metastatic potential.

Karyotype Evolution

Whereas the melan-a cell line displayed no structural aberrations based on SKY analysis, the 2C, 4C, and 4C3– cell lines displayed common structural aberrations of T(8;14), T(14;8), and Fus(8.6). The metastatic melanoma cell line (4C3+) had a more heterogeneous karyotype, indicative of higher instability in the latter cells. Supporting the case for increased genomic instability in the 43C+ cell line, Rb fusions were found in 100% of metaphases analyzed from 4C3+

cells (Figures 5B and W1 and Table 1). Deletions of chromosome 11 were the only shared chromosomal abnormalities among 2C, 4C, 4C3–, and 4C3+ cell lines (Table 1). Whereas the total number of chromosomes increased in the 4C3+ cell line to 72, the number of centromere fragments decreased compared with all other cell lines. In contrast to 4C3+, the 4C3– cell line showed on average fewer chromosomes, 53 per cell, with more centromere fragments ($P < .0001$; Table 1 and Figure 4C).

Discussion

Our group has recently established a melanocyte malignant transformation model where a murine-nontumorigenic melanocyte cell line (melan-a) was submitted to sequential cycles of cell anchorage blockade resulting in the establishment of nontumorigenic melan-a sublines and several melanoma cell lines [31,40]. In melanoma, the possibility of correlating a specific pathological state with several corresponding genetic alterations has allowed the experimental study of different stages of oncogenesis. Our cell adhesion blockage model allows for investigating early stage tumor progression unlike other chemical transformation models or melanoma tissue samples.

Our results suggest that adhesion blockage cycles initiate telomere- and centromere-driven CIN that becomes the causative factors in genomic instability and early tumor development. It is widely supported that telomere dysfunction could play a causal role in early carcinogenesis by instigating bridge-breakage-fusion type chromosomal instabilities, thus promoting neoplastic transformation [43,44].

To study the timing of the occurrence of telomere shortening during melanocyte transformation, we analyzed in our model the profile of telomere length by Q-FISH. We found that telomere length significantly
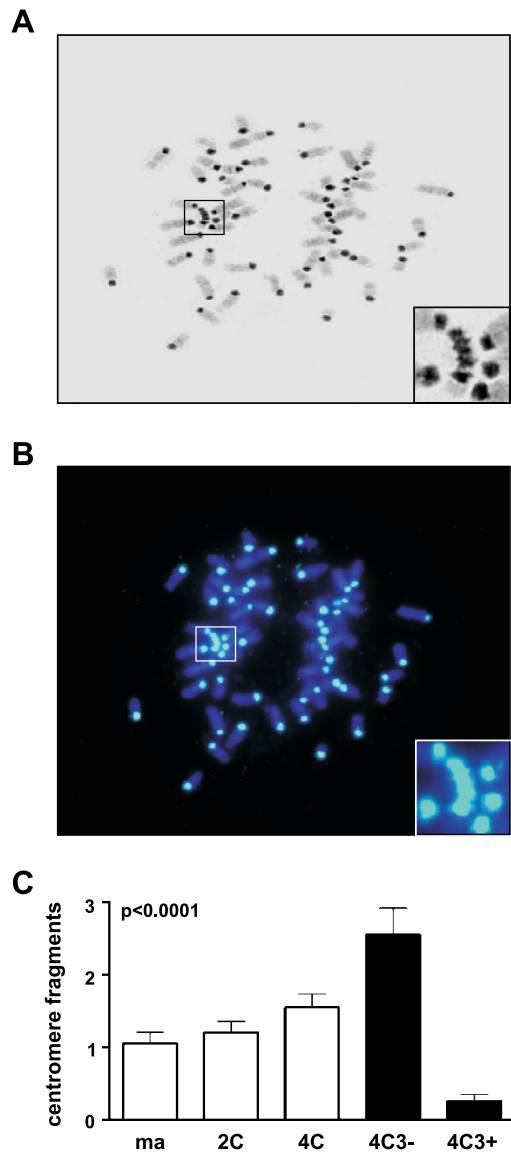
Figure 5. Chromosome rearrangements. A total of 20 metaphases were examined for each cell line. (A) Number of rearrangements found in each cell line per metaphase. (B) Number of Rb chromosome found per metaphase in the melanoma model. (C) Variation in ploidy found in the tumorigenesis model.

Figure 4. Centromere fragments. Multicentric chromosomes and centromere fragments are visible by FISH. Metaphases of 4C3− cell line were hybridized using a mouse pan-centromeric probe conjugated to FITC (green) (Cambio). (A) Inverted DAPI image. (B) Pan-centromeric probe. White squares highlight the centromere fragments, and they are shown on the magnification boxes in both panels. (C) Number of centromere fragments in all the cell lines. Note that the numbers increased from melan-a to 4C3−, almost disappearing on 4C3+. *4C3−* indicates slow-growing melanoma cell line; *4C3+*, fast-growing melanoma cell line.

decreased as additional rounds of cell anchorage blockages were performed. In addition, variation among telomere length for individual cell lines significantly decreased in parallel with telomere length as subsequent cell anchorage blockages were performed. The development of smaller and less variable sized telomeres is described in a multitude of cancers [45]. These findings are in agreement with the idea that telomere length abnormalities seem to be one of the earliest genetic alterations acquired in the multistep process of malignant transformation.

Table 1. Summary of the Rearrangements Found throughout Melanocyte Malignant Transformation.

Cell Line	No. Chromosomes*	Centromere Fragments[†]	Aberration Chart (Structural Aberrations)
melan-a	54	Yes {1}	None
2C	51	Yes {1}	T(8;14){13}/T(14;8){20}/F(8;6){19}/Del(11){18}
4C	51	Yes {1}	T(8;14){19}/T(14;8){21}/T(15;X){18}/F(8;6){4}/Del(11){18}
4C3–	53	Yes {2}	T(8;14){18}/T(14;8){21}/T(5;18){9}/T(15;X){18}/F(8;6){15}/Del(11){17}
4C3+	72	None {0}	T(1;16){18}/T(8;1){17}/T(1;12){15}/T(3;13){20}/T(13;3){20}/T(X;15){19}/ T(10;16){16}/Rb(8.12){15}/Rb(12.12){26}/Del(1){18}/Del(6){12}/Del(11){20}

The data given are derived from the analysis of 20 metaphases. The braces indicate how often each rearrangement was seen in 20 metaphases. Only rearrangements that were present in more than 2 metaphases are presented here.

*Median of chromosome number from 20 metaphases.

[†]Absence or presence of centromere fragments in the metaphases; braces represent the median of fragments found in the cell lines studied.
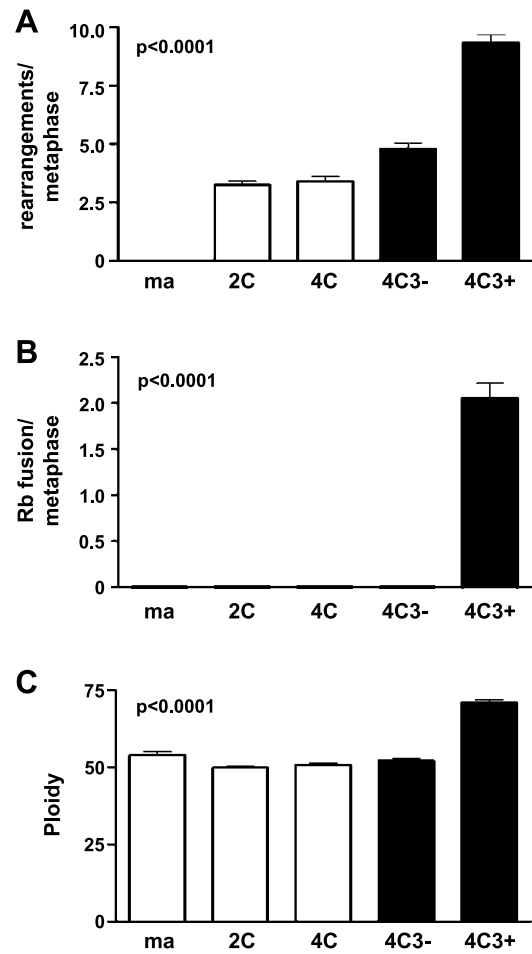
Indeed, telomere shortening and telomerase activation are the most prevalent aberrations in precancerous lesions [46]. Telomere length abnormalities have been described in preinvasive breast lesions [47], pancreas [48], prostate [49–51], and many different types of human epithelial cancer precursor stages [52]. Likewise, telomerase activity has been detected early in carcinogenesis [53–55].

In addition, an *in vivo* study in human breast cancer found that cancer cells continue to experience telomere loss and anaphase bridges even after the expression of telomerase [56]. These data suggest that telomerase expression alone is not sufficient to maintain telomeres at noncritical length. Similarly, in our mouse melanoma model, we observed telomere shortening in parallel to genomic instability in the context of telomerase-positive cell lines. In addition, several lines of evidence suggest a protective function for telomerase apart from its role in telomere elongation [57,58]. In recent work, Xu and Blackburn [59] described a distinct class of extremely short telomeres (t-stumps) in human cancer cells with active telomerase.

Apart from telomere abnormalities, our melanoma displays an abundance of centromeric instability manifested as centromere fragments and centromeric fusions. Those centromere fragments increase from melan-a to 4C3– almost disappearing in 4C3+ where the Rb fusions are present. Many centromeric fragments contained four telomere signals and could be described as mini chromosomes or double minutes. These structures were likely produced by the fusion of two individual centromere fragments where the shortening of telomeres would lead to a telocentric fusion creating two chromosomes with terminal deletions and one centromere fragment with four telomeric signals. This mechanism is supported by the fact that the rate of telomere free ends increases as additional rounds of cell adhesion blockages are performed.

Rb translocations in humans constitute the most common structural genetic abnormalities in aborted fetuses and newborns [60–62]. Moreover, human Rb translocation chromosomes have been found as acquired or constitutional genetic lesions in hematological cancers [63,64] in solid tumors [65,66] and at the onset of acute myelogenous leukemia [67]. The presence of Rb fusions in our model correlates with oncogenesis because the metastatic cell line is the only cell line with the Rb structure.

Our results describe a melanoma model whereby repetitive cycles of cell anchorage blockage generate CIN with a cytological signature of centromere breakage and telomeric loss. This phenotype in immortalized melanocyte melan-a cells that seem to have initial genomic or epigenomic insults. This unique model allows for molecular investigations into the early stages of development for melanoma.

References

[1] Hussein MR (2004). Genetic pathways to melanoma tumorigenesis. *J Clin Pathol* **57**, 797–801.

[2] Lengauer C, Kinzler KW, and Vogelstein B (1998). Genetic instabilities in human cancers. *Nature* **396**, 643–649.

[3] Hussein MR, Sun M, Roggero E, Sudilovsky EC, Tuthill RJ, Wood GS, and Sudilovsky O (2002). Loss of heterozygosity, microsatellite instability, and mismatch repair protein alterations in the radial growth phase of cutaneous malignant melanomas. *Mol Carcinog* **34**, 35–44.

[4] Albertson DG, Collins C, McCormick F, and Gray JW (2003). Chromosome aberrations in solid tumors. *Nat Genet* **34**, 369–376.

[5] Gebhart E and Liehr T (2000). Patterns of genomic imbalances in human solid tumors. *Int J Oncol* **16**, 383–399.

[6] Bayani J, Selvarajah S, Maire G, Vukovic B, Al-Romaih K, Zielenska M, and Squire JA (2007). Genomic mechanisms and measurement of structural and numerical instability in cancer cells. *Semin Cancer Biol* **17**, 5–18.

[7] Yuen KW, Montpetit B, and Hieter P (2005). The kinetochore and cancer: what's the connection? *Curr Opin Cell Biol* **17**, 576–582.

[8] Storchova Z and Pellman D (2004). From polyploidy to aneuploidy, genome instability and cancer. *Nat Rev Mol Cell Biol* **5**, 45–54.

[9] Henikoff S, Ahmad K, and Malik HS (2001). The centromere paradox: stable inheritance with rapidly evolving DNA. *Science* **293**, 1098–1102.

[10] Shaw CJ and Lupski JR (2004). Implications of human genome architecture for rearrangement-based disorders: the genomic basis of disease. *Hum Mol Genet* **1**, R57–R64.

[11] Gonçalves Dos Santos Silva A, Sarkar R, Harizanova J, Guffei A, Mowat M, Garini Y, and Mai S (2008). Centromeres in cell division, evolution, nuclear organization and disease. *J Cell Biochem* **104**, 2040–2058.

[12] Yue Y, Grossmann B, Ferguson-Smith M, Yang F, and Haaf T (2005). Comparative cytogenetics of human chromosome 3q21.3 reveals a hot spot for ectopic recombination in hominoid evolution. *Genomics* **85**, 36–47.

[13] Jamet D, Marzin Y, Douet-Guilbert N, Morel F, Le Bris MJ, Herry A, Banzakour S, Bourquard P, Morice P, Abgrall JF, et al. (2005). Jumping translocations in multiple myeloma. *Cancer Genet Cytogenet* **161**, 159–163.

[14] Chantot-Bastaraud S, Ravel C, Berthaut I, McElreavey K, Bouchard P, Mandelbaum J, and Siffroi JP (2007). Sperm-FISH analysis in a pericentric chromosome 1 inversion, 46,XY,inv(1)(p22q42), associated with infertility. *Mol Hum Reprod* **13**, 55–59.

[15] Collodel G, Moretti E, Capitani S, Piomboni P, Anichini C, Estenoz M, and Baccetti B (2006). TEM, FISH and molecular studies in infertile men with pericentric inversion of chromosome 9. *Andrologia* **38**, 122–127.

[16] Anton E, Blanco J, Egozcue J, and Vidal F (2005). Sperm studies in heterozygote inversion carriers: a review. *Cytogenet Genome Res* **111**, 297–304.

[17] Anelli L, Albano F, Zagaria A, Liso A, Cuneo A, Mancini M, Liso V, Rocchi M, and Specchia G (2004). Pericentric chromosome 8 inversion associated with the 5′RUNX1/3′CBFA2T1 gene in acute myeloid leukemia cases. *Ann Hematol* **84**, 245–249.

[18] Pedrazzini E, Cerretini R, Noriega MF, Narbaitz M, Palacios MF, Negri P, Bengió R, and Slavutsky I (2006). Inversions of chromosomes 2 and 6 in mantle cell lymphoma. Cytogenetic, FISH, and molecular studies. *Cancer Genet Cytogenet* **167**, 164–167.

[19] Mathew S, Dalton J, Riedley S, Spunt SL, and Hill DA (2002). Complex t(X;18)(p11.2;q11.2) with a pericentric inversion of the X chromosome in an adolescent boy with synovial sarcoma. *Cancer Genet Cytogenet* **132**, 136–140.

[20] Ulucan H, Akin R, Kösem M, and Gül D (2006). *De novo* pericentric inversion of chromosome 5 in a girl with mental retardation and unilateral ear malformation. *Am J Med Genet A* **140**, 298–299.

[21] Ramadevi AR, Naik U, Dutta U, Srikanth, and Prabhakara K (2002). *De novo* pericentric inversion of chromosome 4, inv(4)(p16q12) in a boy with piebaldism and mental retardation. *Am J Med Genet* **113**, 190–192.

[22] Bailey S and Murnane JP (2006). Telomeres, chromosome instability and cancer. *Nucl Acid Res* **34**, 2408–2417.

[23] Desmaze C, Soria JC, Freulet-Marriere MA, Mathieu N, and Sabatier L (2003). Telomere-driven genomic instability in cancer cells. *Cancer Lett* **194**, 173–182.

[24] Riha K, Heacock ML, and Shippen DE (2006). The role of the nonhomologous end-joining DNA double-strand break repair pathway in telomere biology. *Annu Rev Genet* **40**, 237–277.

[25] Louis SF, Vermolen BJ, Garini Y, Young IT, Guffei A, Lichtensztejn Z, Kuttler F, Chuang TC, Moshir S, Mougey V, et al. (2005). c-Myc induces chromosomal rearrangements through telomere and chromosome remodeling in the interphase nucleus. *Proc Natl Acad Sci USA* **102**, 9613–9618.

[26] Mai S and Garini Y (2005). Oncogenic remodeling of the threedimensional organization of the interphase nucleus: c-Myc induces telomeric aggregates whose formation precedes chromosomal rearrangements. *Cell Cycle* **4**, 1327–1331.

[27] Caporali A, Wark L, Vermolen BJ, Garini Y, and Mai S (2007). Telomeric aggregates and end-to-end chromosomal fusions require myc box II. *Oncogene* **26**, 1398–1406.

[28] Guffei A, Lichtensztejn Z, Gonçalves Dos Santos Silva A, Louis SF, Caporali A, and Mai S (2007). c-Myc-dependent formation of Robertsonian translocation chromosomes in mouse cells. *Neoplasia* **9**, 578–588.

[29] Foijer F, Draviam VM, and Sorger PK (2008). Studying chromosomal instability in the mouse. *Biochim Biophys Acta* **1786**, 73–82.

[30] Wu X and Pandolfi PP (2001). Mouse models for multistep tumorigenesis. *Trends Cell Biol* **11**, S2–S9.

[31] Oba-Shinjo SM, Correa M, Ricca TI, Molognoni F, Pinhal MA, Neves IA, Marie SK, Sampaio LO, Nader HB, Chammas R, et al. (2006). Melanocyte transformation associated with substrate adhesion impediment. *Neoplasia* **8**, 231–241.

[32] Bennett DC, Cooper PJ, and Hart IR (1987). A line of non-tumorigenic mouse melanocytes, syngeneic with the B16 melanoma and requiring a tumour promoter for growth. *Int J Cancer* **39**, 414–418.

[33] Mai S and Wiener F (2002). Murine FISH. *FISH: A Practical Approach.* B Beatty, S Mai, and J Squire (Eds.). Oxford, UK: Oxford University Press, pp. 55–67.

[34] Garagna S, Zuccotti M, Thornhill A, Fernandez-Donoso R, Berrios S, Capanna E, and Redi CA (2001). Alteration of nuclear architecture in male germ cells of chromosomally derived subfertile mice. *J Cell Sci* **114**, 4429–4434.

[35] Schaefer LH, Schuster D, and Herz H (2001). Generalized approach for accelerated maximum likelihood based image restoration applied to three-dimensional fluorescence microscopy. *J Microsc* **204**, 99–107.

[36] Chuang TC, Moshir S, Garini Y, Chuang AY, Young IT, Vermolen B, van den Doel R, Mougey V, Perrin M, Braun M, et al. (2004). The three-dimensional organization of telomeres in the nucleus of mammalian cells. *BMC Biol* **3**, 2–12.

[37] Vermolen BJ, Garini Y, Mai S, Mougey V, Fest T, Chuang TC, Chuang AY, Wark L, and Young IT (2005). Characterizing the three-dimensional organization of telomeres. *Cytometry A* **67**, 144–150.

[38] Cleveland DW, Mao Y, and Sullivan KF (2003). Centromeres and kinetochores: from epigenetics to mitotic checkpoint signaling. *Cell* **112**, 407–421.

[39] Dalla Torre CA, Maciel RM, Pinheiro NA, Andrade JA, De Toledo SR, Villa LL, and Cerutti JM (2002). TRAP-silver staining, a highly sensitive assay for measuring telomerase activity in tumor tissue and cell lines. *Braz J Med Biol Res* **35**, 65–68.

[40] Correa M, Machado J Jr, Carneiro CR, Pesquero JB, Bader M, Travassos LR, Chammas R, and Jasiulionis MG (2005). Transient inflammatory response induced by apoptotic cells is an important mediator of melanoma cell engraftment and growth. *Int J Cancer* **114**, 356–363.

[41] Kanaya T, Kyo S, Takakura M, Ito H, Namiki M, and Inoue M (1998). hTERT is a critical determinant of telomerase activity in renal-cell carcinoma. *Int J Cancer* **78**, 539–543.

[42] Kolquist KA, Ellisen LW, Counter CM, Meyerson M, Tan LK, Weinberg RA, Haber DA, and Gerald WL (1998). Expression of TERT in early permalignant lesions and a subset of cells in normal tissues. *Nat Genet* **19**, 182–186.

[43] Soler D, Genescà A, Arnedo G, Egozcue J, and Tusell L (2005). Telomere dysfunction drives chromosomal instability in human mammary epithelial cells. *Genes Chromosomes Cancer* **44**, 339–350.

[44] Artandi SE, Chang S, Lee SL, Alson S, Gottlieb GJ, Chin L, and DePinho RA (2000). Telomere dysfunction promotes non-reciprocal translocations and epithelial cancers in mice. *Nature* **406**, 641–645.

[45] Londoño-Vallejo JA (2008). Telomere instability and cancer. *Biochimie* **90**, 73–82.

[46] Raynaud CM, Sabatier L, Philipot O, Olaussen KA, and Soria JC (2008). Telomere length, telomeric proteins and genomic instability during the multistep carcinogenic process. *Crit Rev Oncol Hematol* **66**, 99–117.

[47] Meeker AK and Argani P (2004). Telomere shortening occurs early during breast tumorigenesis: a cause of chromosome destabilization underlying malignant transformation? *J Mammary Gland Biol Neoplasia* **9**, 285–296.

[48] van Heek NT, Meeker AK, Kern SE, Yeo CJ, Lillemoe KD, Cameron JL, Offerhaus GJ, Hicks JL, Wilentz RE, Goggins MG, et al. (2002). Telomere shortening is nearly universal in pancreatic intraepithelial neoplasia. *Am J Pathol* **161**, 1541–1547.

[49] Joshua AM, Evans A, Van der Kwast T, Zielenska M, Meeker AK, Chinnaiyan A, and Squire JA (2008). Prostatic preneoplasia and beyond. *Biochim Biophys Acta* **1785**, 156–181.

[50] Vukovic B, Beheshti B, Park P, Lim G, Bayani J, Zielenska M, and Squire JA (2007). Correlating breakage-fusion-bridge events with the overall chromosomal instability and *in vitro* karyotype evolution in prostate cancer. *Cytogenet Genome Res* **116**, 1–11.

[51] Meeker AK, Hicks JL, Platz EA, March GE, Bennett CJ, Delannoy MJ, and De Marzo AM (2002). Telomere shortening is an early somatic DNA alteration in human prostate tumorigenesis. *Cancer Res* **62**, 6405–6409.

[52] Meeker AK, Hicks JL, Iacobuzio-Donahue CA, Montgomery EA, Westra WH, Chan TY, Ronnett BM, and De Marzo AM (2004). Telomere length abnormalities occur early in the initiation of epithelial carcinogenesis. *Clin Cancer Res* **10**, 3317–3326.

[53] Lantuejoul S, Soria JC, Morat L, Lorimier P, Moro-Sibilot D, Sabatier L, Brambilla C, and Brambilla E (2005). Telomere shortening and telomerase reverse transcriptase expression in preinvasive bronchial lesions. *Clin Cancer Res* **11**, 2074–2082.

[54] Gulmann C, Lantuejoul S, Grace A, Leader M, Patchett S, and Kay E (2005). Telomerase activity in proximal and distal gastric neoplastic and preneoplastic lesions using immunohistochemical detection of hTERT. *Dig Liver Dis* **37**, 439–445.

[55] Lancelin F, Anidjar M, Villette JM, Soliman A, Teillac P, Le Duc A, Fiet J, and Cussenot O (2000). Telomerase activity as a potential marker in preneoplastic bladder lesions. *BJU Int* **85**, 526–531.

[56] Chin K, de Solorzano CO, Knowles D, Jones A, Chou W, Rodriguez EG, Kuo WL, Ljung BM, Chew K, Myambo K, et al. (2004). *In situ* analysis of genome instability in breast cancer. *Nat Genet* **16**, 984–988.

[57] Kim M, Xu L, and Blackburn EH (2003). Catalytically active human telomerase mutants with allele-specific biological properties. *Exp Cell Res* **288**, 277–287.

[58] Zhu J, Wang H, Bishop JM, and Blackburn EH (1999). Telomerase extends the lifespan of virus-transformed human cells without net telomere lengthening. *Proc Natl Acad Sci USA* **96**, 3723–3728.

[59] Xu L and Blackburn EH (2007). Human cancer cells harbor T-stumps, a distinct class of extremely short telomeres. *Mol Cell* **28**, 315–327.

[60] Kim SR and Shaffer LG (2002). Robertsonian translocations: mechanisms of formation, aneuploidy, and uniparental disomy and diagnostic considerations. *Genet Test* **6**, 163–168.

[61] Nielsen J and Wohlert M (1991). Chromosome abnormalities found among 34,910 newborn children: results from a 13-year incidence study in Arhus, Denmark. *Hum Genet* **87**, 81–83.

[62] Jacobs PA (1981). Mutation rates of structural chromosome rearrangements in man. *Am J Hum Genet* **33**, 44–54.

[63] Welborn J (2004). Acquired Robertsonian translocations are not rare events in acute leukemia and lymphoma. *Cancer Genet Cytogenet* **151**, 14–35.

[64] Qian J, Xue Y, Sun J, Guo Y, Pan J, Wu Y, Wang W, and Yao L (2002). Constitutional Robertsonian translocations in (9;22)-positive chronic myelogenous leukemia. *Cancer Genet Cytogenet* **132**, 79–80.

[65] Bayani J, Zielenska M, Pandita A, Al-Romaih K, Karaskova J, Harrison K, Bridge JA, Sorensen P, Thorner P, and Squire JA (2003). Spectral karyotyping identifies recurrent complex rearrangements of chromosomes 8, 17, and 20 in osteosarcomas. *Genes Chromosomes Cancer* **36**, 7–16.

[66] Padilla-Nash HM, Heselmeyer-Haddad K, Wangsa D, Zhang H, Ghadimi BM, Macville M, Augustus M, Schröck E, Hilgenfeld E, and Ried T (2001). Jumping translocations are common in solid tumor cell lines and result in recurrent fusions of whole chromosome arms. *Genes Chromosomes Cancer* **30**, 349–363.

[67] Shimokawa T, Sakai M, Kojima Y, and Takeyama H (2004). Acute myelogeneous leukemia (M5a) that demonstrated chromosomal abnormality of Robertsonian 13;21 translocation at onset. *Intern Med* **43**, 508–511.
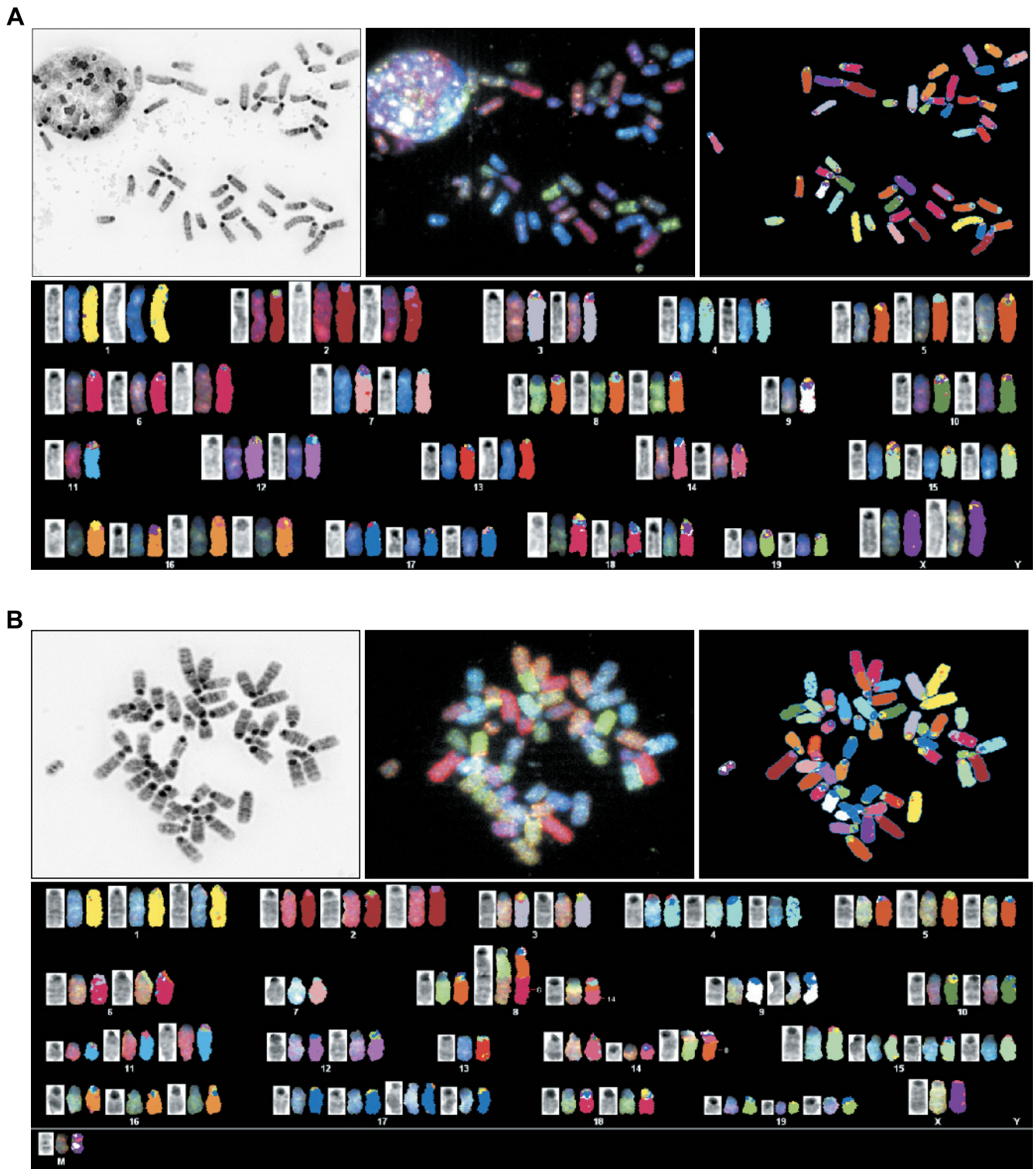
Figure W1. Karyotype evolution. SKY of metaphases derived from cell lines corresponding to phases of melanocyte malignant transformation. Representative images from SKY are shown: (A) melan-a, (B) 2C, (C) 4C, (D) 4C3−, and (E) 4C3+. White arrows point to Rb fusion chromosomes. Note the increase of abnormalities through the model and the increase of chromosome number in the 4C3+ cell line. Each panel shows a representative image for each cell type; however, the layout is the same for all. Left panel: the raw image of a metaphase; central panel: the classified image of the metaphase; right panel: the inverted DAPI-banded image of the metaphase; and larger panel: the karyotype table of the metaphase. *ma* indicates melan-a cells; *2C and 4C*, melan-a cells submitted to two and four substrate adhesion blockade cycles, respectively; *4C3−*, slow-growing melanoma cell line; *4C3+*, fast-growing melanoma cell line.
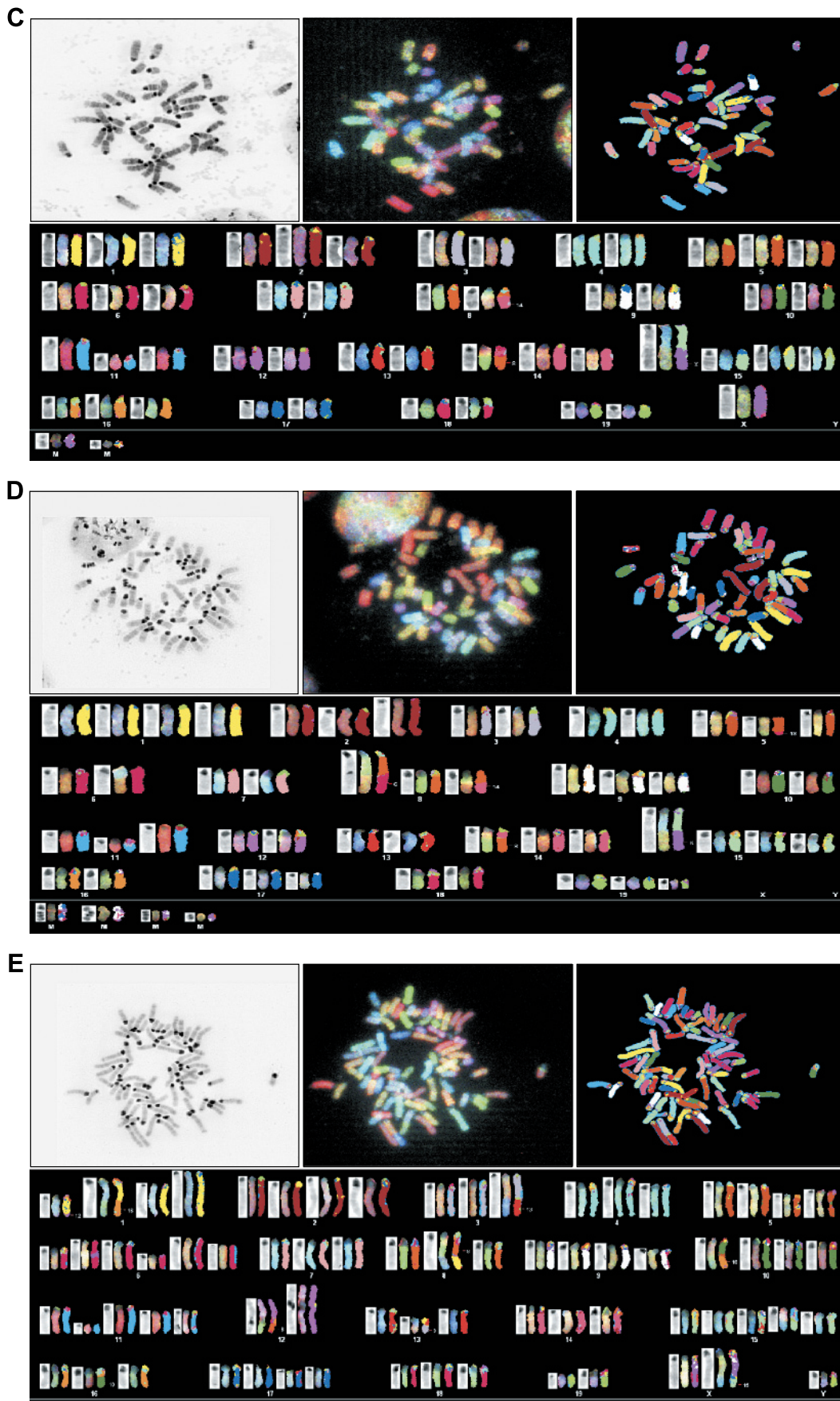
C

D

E
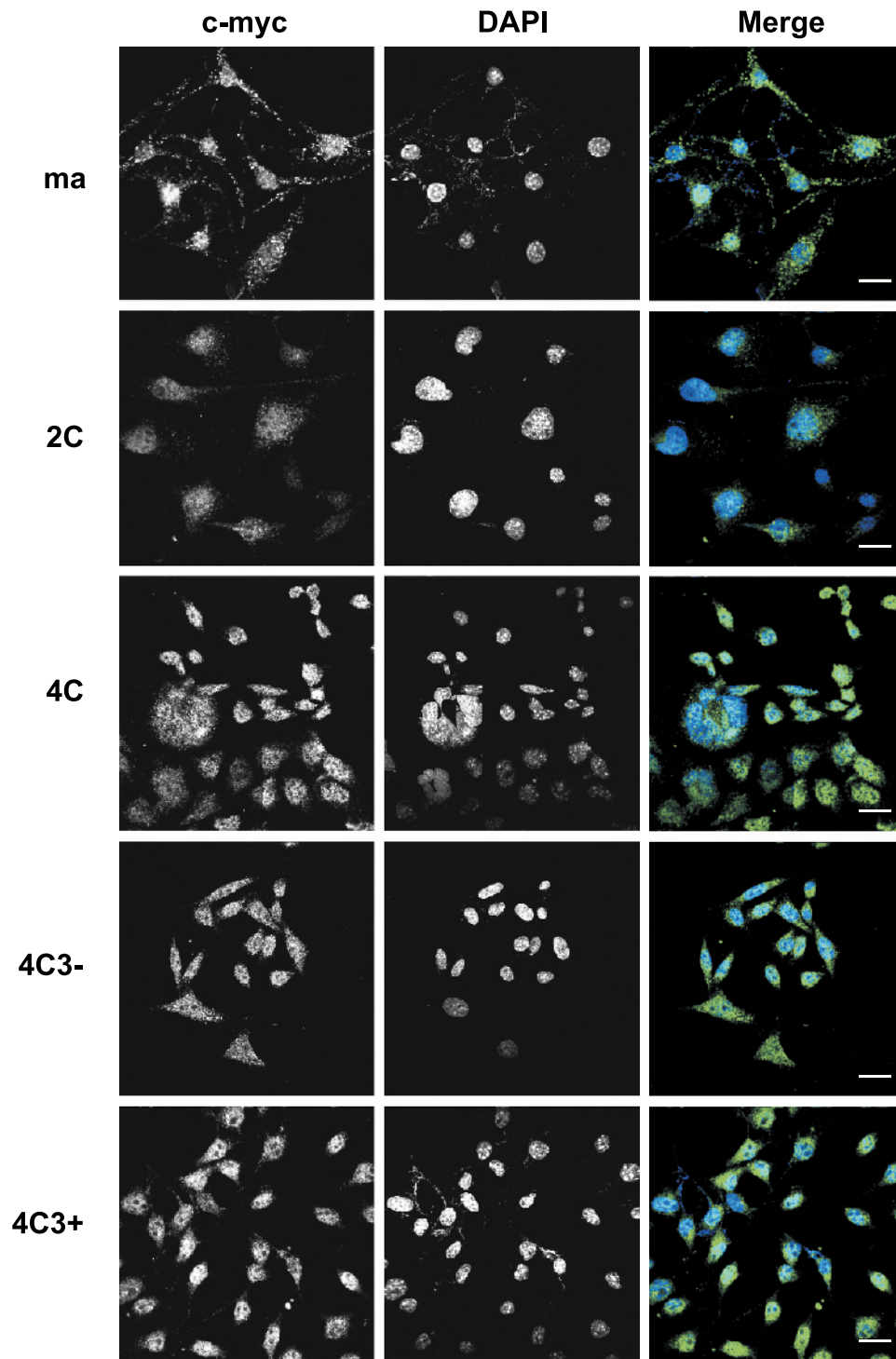

Figure W1. (*continued*).

Figure W2. Indirect immunofluorescence using a c-Myc–specific antibody. c-Myc staining in the melanoma model. Each panel shows a representative image for each cell type; however, the layout is kept constant. Left column: c-Myc staining (N262; Santa Cruz Biotechnology); central column: nuclear staining (DAPI); right column: merge images. *ma* indicates melan-a cells; *2C and 4C*, melan-a cells submitted to two and four substrate adhesion blockade cycles, respectively; *4C3−*, slow-growing melanoma cell line; *4C3+*, fast-growing melanoma cell line. Bars, 20 μm.

Table W1. Summary of Chromosomes Involved in the Formation of Rb Chromosomes in 4C3+ Cells in a Nonrandom Manner.

Chromosome Number	Times Involved in Rb Fusions	P
8	15	<.01
12	67	<.001

The numbers given are derived from the analysis of 20 metaphases. All metaphases carried at least one Rb chromosome, fifteen of these 20 metaphases carried two or more Rb fusions. The involvement of each chromosome in the formation of Rb chromosomes is given, and the respective significance is indicated. Fifteen of twenty metaphases (75%) carried one Rb fusion involving chromosomes 8 and 12, whereas 100% of the metaphases analyzed carried at least one Rb(12.12). For further details, see text and Materials and Methods section.